

**UCC Library and UCC researchers have made this item openly available.
Please [let us know](#) how this has helped you. Thanks!**

Title	Elucidating structure-property relationships in the design of metal nanoparticle catalysts for the activation of molecular oxygen
Author(s)	Hinde, Christopher S.; Ansovini, Davide; Wells, Peter P.; Collins, Gillian; Van Aswegen, Sivan; Holmes, Justin D.; Hor, T. S. Andy; Raja, Robert
Publication date	2015-05-14
Original citation	Hinde, C. S., Ansovini, D., Wells, P. P., Collins, G., Aswegen, S. V., Holmes, J. D., Hor, T. S. A. and Raja, R. (2015) 'Elucidating Structure–Property Relationships in the Design of Metal Nanoparticle Catalysts for the Activation of Molecular Oxygen', ACS Catalysis, 5(6), pp. 3807-3816. doi: 10.1021/acscatal.5b00481
Type of publication	Article (peer-reviewed)
Link to publisher's version	https://pubs.acs.org/doi/10.1021/acscatal.5b00481 http://dx.doi.org/10.1021/acscatal.5b00481 Access to the full text of the published version may require a subscription.
Rights	© 2015 American Chemical Society. This document is the Accepted Manuscript version of a Published Work that appeared in final form in ACS Catalysis, copyright © American Chemical Society after peer review and technical editing by the publisher. To access the final edited and published work see https://pubs.acs.org/doi/10.1021/acscatal.5b00481
Item downloaded from	http://hdl.handle.net/10468/6580

Downloaded on 2021-11-27T06:36:19Z

1 Elucidating Structure–Property Relationships in the Design of Metal 2 Nanoparticle Catalysts for the Activation of Molecular Oxygen

3 Christopher S. Hinde,^{†,‡} Davide Ansovini,[†] Peter P. Wells,^{#,Δ} Gillian Collins,^{||,⊥} Sivan Van Aswegen,[†]
4 Justin D. Holmes,^{||,⊥} T. S. Andy Hor,^{‡,§} and Robert Raja^{*,†}

5 [†]School of Chemistry, University of Southampton, Southampton SO17 1BJ, U.K.,

6 [‡]Institute of Materials Research and Engineering (IMRE), A*STAR, 3 Research Link, Singapore 117602

7 [#]UK Catalysis Hub, Research Complex at Harwell, Harwell, Oxon OX11 0FA, U.K.

8 ^ΔKathleen Lonsdale Building, Department of Chemistry, University College London, Gordon Street, London WC1H 0AJ, U.K.

9 ^{||}Department of Chemistry and Tyndall National Institute, University College Cork, Cork, Ireland

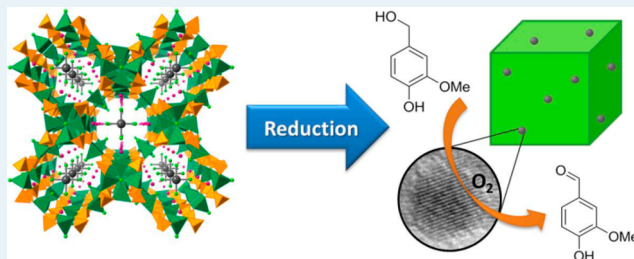
10 [⊥]Centre for Research on Adaptive Nanostructures and Nanodevices (CRANN), Trinity College Dublin, Dublin 2, Ireland

11 [§]Department of Chemistry, National University of Singapore, 3 Science Drive 3, Singapore 117543

12 **S** Supporting Information

13 **ABSTRACT:** A novel synthetic strategy for the design of metal
14 nanoparticles by extrusion of anionic chloride precursors from a
15 porous copper chlorophosphate framework has been devised
16 for the sustainable aerobic oxidation of vanillyl alcohol (4-
17 hydroxy-3-methoxybenzyl alcohol) to vanillin (4-hydroxy-3-
18 methoxybenzaldehyde) using a one-step, base-free method. The
19 precise nature of the Au, Pt, and Pd species has been elucidated
20 for the as-synthesized and thermally activated analogues, which
21 exhibit fascinating catalytic properties when subjected to diverse
22 activation environments. By employing a combination of
23 structural and spectroscopic characterization tools, it has been shown that analogous heat treatments have differing effects on
24 extrusion of a particular metal species. The most active catalysts in this series of materials were the extruded Pt nanoparticles that
25 were generated by reduction in H₂, which exhibit enhanced catalytic behavior, when compared to its Au or Pd counterparts, for
26 industrially significant, aerobic oxidation reactions.

27 **KEYWORDS:** nanoparticle, catalysis, vanillyl alcohol, structure–property correlations, aerobic oxidation, vanillin, EXAFS



28 ■ INTRODUCTION

29 Design of versatile metal nanoparticle (NP) catalysts has been a
30 progressive area of research within the field of heterogeneous
31 catalysis in recent years, due to their significant potential in a
32 variety of chemical transformations, including industrially
33 desirable selective aerobic oxidations. Monometallic (Au, Pt,
34 Pd) and bimetallic NPs have been successfully employed in the
35 selective oxidation of alcohols,¹ including glycerol,² cinnamyl
36 alcohol,³ crotyl alcohol^{4,5} and benzyl alcohol,^{6,7} to name but a
37 few. Prodigious design of bimetallic equivalents has recently
38 demonstrated their propensity for C–H activation, particularly
39 in the oxidation of aromatics.^{8,9} In addition to bulk chemical
40 applications, heterogenized Pd NPs have also found a niche for
41 cross-coupling reactions, alongside their ubiquitous homo-
42 geneous counterparts.¹⁰ The key to engineering catalytically
43 active NPs reproducibly appears to be contingent on the
44 development of robust design strategies that can control the
45 size and shape of the particles at the nanoscale, which still
46 proves to be a challenge.¹¹

47 A variety of preparation methods for generating NPs on solid
48 supports have been previously studied with specific focus on

control of the nanoparticle size and shape.^{11–14} These include 49
wet impregnation,¹⁵ deposition–precipitation¹⁶ and sol– 50
immobilization techniques,^{17,18} with the latter showing a 51
greater propensity for the generation of smaller particle sizes, 52
but often resulting in polymer-capped particulates and hence a 53
reduction in accessible surface area. More importantly, these 54
research efforts have clearly illustrated that changes in size, 55
ranging from average diameters of less than 1 nm up to 10 nm, 56
can have a substantial effect on catalytic activity,^{11,12,19} with 57
smaller particle sizes affording superior conversion rates in most 58
cases. In fact, studies involving cluster-based nanoparticle 59
catalysts even highlighted the integral importance of site- 60
isolation as well as particle size in enhancing efficiency of 61
catalytic oxidations and hydrogenations.^{20–25} The nature of 62
support materials has ranged from metal oxides²⁶ and 63
carbonaceous materials,²⁷ to microporous alternatives such as 64
zeolites^{28,29} or metal–organic frameworks (MOFs),^{30,31} and 65

Received: March 6, 2015

Revised: April 10, 2015

66 mesoporous silica-derived hosts³² such as MCM-41 or SBA-15.
 67 Nanoporous materials have been extensively explored for their
 68 intrinsic catalytic properties;³³ however, isolated single-sites in
 69 the form of doped frameworks^{34–36} or supported nanoparticles
 70 have proved to be superior. The latter have afforded a better
 71 understanding of the nature of the active site at the molecular
 72 level, which has resulted in the development of heterogenized
 73 NP catalysts with unprecedented activity.^{21–24}
 74 We have recently demonstrated a novel strategy for
 75 generating uniform sized, small NPs (ca. 5 nm) by extrusion
 76 of MCl_x precursor complex anions ($M = Au, Pt$ or Pd) from a
 77 crystalline microporous copper chlorophosphate framework
 78 (Figure 1).⁷ The framework is of Cu-2 topology³⁷ and has

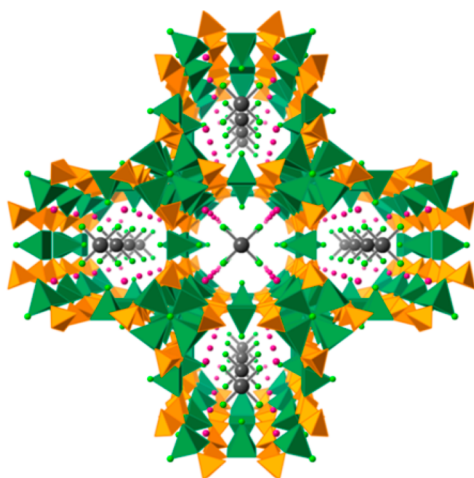
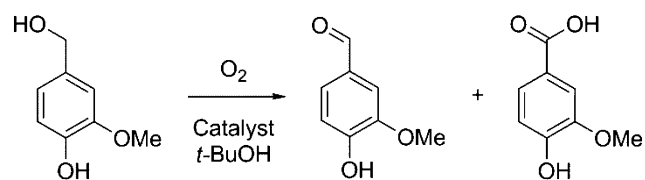


Figure 1. Representative crystal structure of the $[PtCl_4]^{2-}$ supported $Rb_9Cu_6(P_2O_7)_4Cl_2$ framework (Pt – gray spheres, Cl – green spheres, Rb – pink spheres, Cu – green polyhedra, P – orange polyhedra, oxygen omitted for clarity).

79 flexible anion-exchange properties.³⁸ In this article, we
 80 rationalize and demonstrate the efficacy of our design strategy
 81 for the in situ generation of nanoparticles within a microporous
 82 host architecture, wherein the porous framework can be
 83 employed synergistically as an active species, and not just as
 84 a heterogeneous support, thereby affording exciting prospects
 85 for bifunctional catalysis. We have meticulously probed the
 86 nature of the active site using a combination of X-ray
 87 absorption spectroscopy (XAS), X-ray photoelectron spectroscopy
 88 (XPS), and transmission electron microscopy (TEM), for
 89 affording structure–property correlations, which highlight the
 90 efficacy of catalyst activation protocols on metal (NP) extrusion
 91 and ensuing catalytic activity. These findings further confirmed
 92 the structural and compositional integrity of the active sites,
 93 that subsequently led to the design and creation of well-defined
 94 and isolated heterogeneous NP catalysts for the aerobic
 95 oxidation of vanillyl alcohol (Scheme 1), using a one-step,
 96 base-free method.

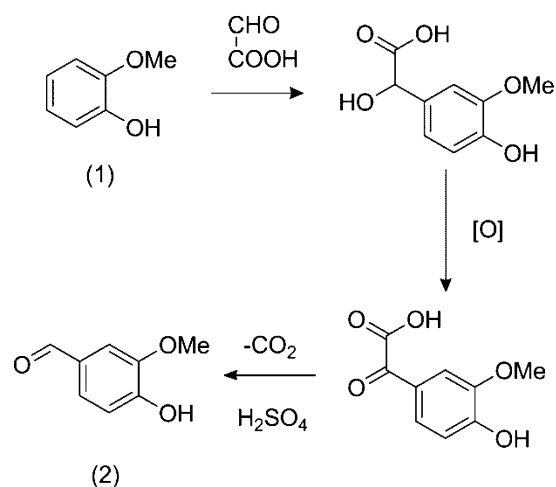
97 The production of vanillin is significant in the fine chemicals
 98 industry, as its primary use in vanilla flavorings and fragrances
 99 make it the single-most highly produced additive in this field.³⁹
 100 Demand for food-grade vanillin has led to a production rate of
 101 approximately 12 000 tons per annum, of which natural vanilla
 102 extracts contribute only 20 tons.⁴⁰ It is also used in other
 103 industries, including as an intermediate toward pharmaceuticals
 104 such as L-3,4-dihydroxy-phenylalanine (L-DOPA), a key
 105 therapeutic agent used to combat Parkinson's disease. Current

Scheme 1. Aerobic Oxidation of Vanillyl Alcohol to Vanillin and Vanillic Acid

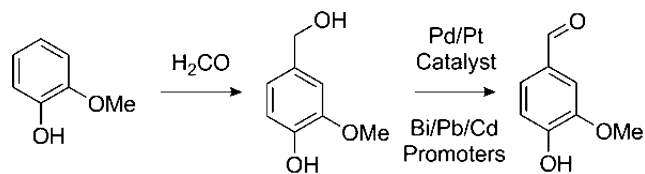


synthetic methods employ one of three routes: (i) an
 established method that utilizes the degradation of lignins,
 which is a solvent intensive process involving multiple
 extraction and distillation steps;⁴⁰ (ii) a cheaper synthetic
 pathway from guaiacol (Schemes 2 and 3), but which involves

Scheme 2. Industrial Synthetic Procedure for Synthesis of Vanillin (2) from Guaiacol (1) via Glyoxylic Acid⁴⁰



Scheme 3. Industrial Synthetic Procedure for Synthesis of Vanillin from Guaiacol via Formaldehyde (See SI)⁴¹



the use of mineral acids and heavy-metal promoters such as Pb,
 Bi, and/or Cd;^{40,41} or (iii) a biosynthetic pathway, which
 involves high production costs.^{42,43} Schemes 2 and 3 represent
 the processes mostly employed in industry today, both of which
 are composed of the same principles: first, a condensation
 reaction with either glyoxylic acid (Scheme 2) or formaldehyde
 (Scheme 3), followed by an oxidation step and subsequent
 decarboxylation. The route via glyoxylic acid requires the
 decarboxylation step to form the desired product, vanillin. The
 formaldehyde route, however, produces small quantities of
 vanillin (16%) after the oxidation step, with the decarboxylation
 converting some of the overoxidation products back to vanillin,
 in order to obtain an overall yield of 61%⁴¹ (detailed scheme in
 Figure S1.1). It is to be noted that both methods involve
 multistep processes to achieve these yields.

The catalytic activation of molecular oxygen is therefore of
 significant interest and poses a substantial challenge for the
 fine-chemicals industry; this is especially true in selective

129 oxidations, with the selective oxidation of vanillyl alcohol to
 130 vanillin being a compelling example. Due to the benign nature
 131 of molecular oxygen, its utilization as a potential oxidant⁴⁴ can
 132 help mitigate the use of hazardous reagents, which lead to the
 133 generation of greenhouse gases and wasteful byproducts
 134 (Schemes 2 and 3).⁴⁵ From an academic and industrial
 135 standpoint, the concomitant use of a heterogeneous catalyst
 136 with molecular oxygen affords many advantages from a socio-
 137 economic and environmental perspective, as it offers a viable
 138 alternative to homogeneous processes that currently generate
 139 stoichiometric quantities of toxic inorganic waste,⁴⁶ thereby
 140 impeding the atom-efficient synthesis of fine-chemicals and
 141 pharmaceuticals.

142 ■ EXPERIMENTAL SECTION

143 Chemicals for synthesis and catalytic tests were purchased from
 144 Sigma-Aldrich, Fisher Scientific, or Acros Organics and used
 145 without further purification.

146 **Material Synthesis.** Copper(II) fluoride (0.1168 g, 1.150
 147 mmol), 85 wt % orthophosphoric acid (0.2 mL, 2.922 mmol),
 148 50 wt % RbOH (0.24 mL, 2.037 mmol), RbCl (0.28 g, 2.316
 149 mmol) and a source of MCl_x ; $H AuCl_4$ (0.0489 g, 0.144 mmol),
 150 K_2PtCl_4 (0.0515 g, 0.124 mmol) or K_2PdCl_4 (0.0405 g, 0.124
 151 mmol) were mixed in the Teflon liner of a custom-made 23 mL
 152 hydrothermal vessel. The vessel was sealed and heated to 448 K
 153 for 2 days.

154 Products formed as brilliant green cuboid crystals for both
 155 the Au and Pt material and as light brown crystals for the Pd
 156 material. Materials were further activated either by calcination
 157 (air, 773 K, 2 h) or reduction (5% H_2/N_2 , 473 K, 2 h) to
 158 generate the active nanoparticle catalysts. After calcination, the
 159 Au and Pd materials appeared unchanged in color, but the Pt
 160 catalyst changed to a darker khaki-green. After reduction, the
 161 Au material appeared unchanged, the Pt material appeared a
 162 more dark green color than the calcined equivalent, and the Pd
 163 material appeared black in color.

164 **X-ray Photoelectron Spectroscopy.** XPS analysis was
 165 performed using a Thermo Scientific Theta Probe instrument
 166 equipped with monochromated Al $K\alpha$ source in NEXUS,
 167 University of Newcastle. A flood gun was used for charge
 168 compensation. A pass energy of 200 eV and a step size of 1.0
 169 eV was employed for all survey spectra while a pass energy of
 170 40 eV and a step size of 0.1 eV was used for high-resolution
 171 spectra of the elements of interest. All XPS spectra were
 172 calibrated against the carbon and/or oxygen 1s peaks, and high-
 173 resolution spectra were fitted with Shirley backgrounds before
 174 peak analysis using the CasaXPS software.⁴⁷

175 **X-ray Absorption Spectroscopy.** Pd, Pt, and Au XAFS
 176 studies were carried out on the B18 beamline at the Diamond
 177 Light Source, Didcot, U.K. Measurements were performed
 178 using a quick extended X-ray absorption fine structure
 179 (QEXAFS) setup with a fast-scanning Si (111) or Si (311)
 180 double crystal monochromator. The normal time resolution of
 181 the spectra reported herein was 1 min/spectrum ($k_{max} = 16$);
 182 on average, six scans were acquired to improve the signal-to-
 183 noise level of the data. All samples were diluted with cellulose
 184 and pressed into pellets to optimize the effective edge-step of
 185 the XAFS data and measured in transmission mode using ion
 186 chamber detectors. All transmission XAFS spectra were
 187 acquired concurrently with the appropriate reference foil placed
 188 between I_t and I_{ref} . XAS data processing and EXAFS analysis
 189 were performed using IFEFFIT⁴⁸ with the Horae package⁴⁹
 190 (Athena and Artemis). The amplitude reduction factor, s_0^2 , was

derived from EXAFS data analysis of known compounds and
 used as a fixed input parameter.

Transmission Electron Microscopy. TEM analysis was
 performed on a Jeol 2100 Electron Microscope at an operating
 voltage of 200 kV. The catalyst framework was prone to
 damage by the electron beam. Therefore, to minimize sample
 degradation, the TEM images were collected quickly to mitigate
 the above.

Catalysis. Catalytic reactions were carried out in a 75 mL
 PTFE lined, stainless-steel, high-pressure batch reactor. The
 reactor was charged with vanillyl alcohol (1 g), diethylene
 glycol dimethyl ether (0.85 g) as an internal standard, *tert*-
 butanol (30 mL) as a solvent and catalyst (50 mg). The reactor
 was pressurized with ≈ 20 bar of dry air, stirred, and heated for
 the required amount of time. Small aliquots of the reaction
 mixture were taken carefully periodically for GC analysis.
 Samples were analyzed by GC (PerkinElmer, Clarus 480) using
 an Elite-5 column equipped with a flame ionization detector
 (FID). Products were identified against authenticated standards
 and quantified by calibration to obtain response factors (R_F)
 against the known internal standard.

192 ■ RESULTS AND DISCUSSION

Figure 2 shows the non-phase-corrected Fourier transform
 (both magnitude and imaginary component) of the k^3 weighted
 EXAFS data for the reduced Pd, Pt, and Au catalyst materials,
 with the fitting parameters generated detailed in Table 1. The
 EXAFS data of the reduced Pt sample is consistent with that
 expected for Pt nanoparticles. The long-range structure in the

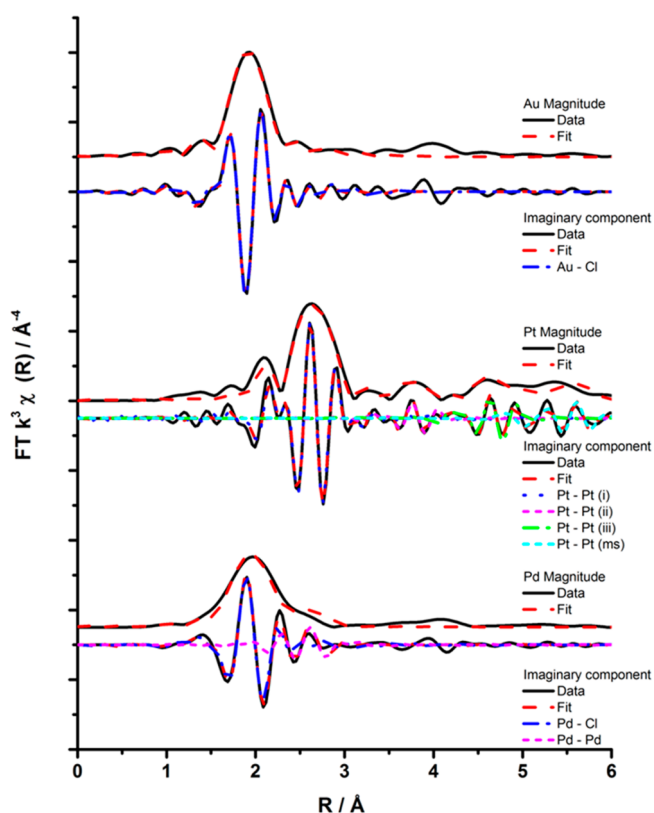


Figure 2. Magnitude and imaginary component of the k^3 weighted Fourier transform for the EXAFS data of the reduced Pd (bottom), Pt (middle), and Au (top) samples. Associated scattering paths are included for the imaginary component.

Table 1. EXAFS Fitting Parameters for the Reduced Pd, Pt and Au Samples^a

sample	abs sc	N	R/Å	2σ ² /Å ²	E _i /eV	R _{factor}
reduced Au sample	Au–Cl	3.7 (2)	2.29 (1)	0.002 (1)	10 (1)	0.005
reduced Pd sample	Pd–Cl	3.3 (3)	2.35 (1)	0.003 (1)	10 (2)	0.004
	Pd–Pd	1.3 (5)	2.77 (2)	0.004 (2)		
reduced Pt sample	Pt–Pt	8.4 (5)	2.76 (1)	0.005 (1)	7 (2)	0.007
	Pt–Pt	3 (1)	3.91 (2)	0.005 (1)		
	Pt–Pt	10 (3)	4.79 (2)	0.007 (1)		
	Pt–Pt (ms)	13 (3)	5.65 (2)	0.011 (2)		

^aFitting parameters: (Au sample) $S_0^2 = 0.75$ as deduced by KAuCl₄ standard; Fit range $3.5 < k < 12.5$, $1.1 < R < 3$; no. of independent points = 10; (Pd sample) $S_0^2 = 0.82$ as deduced by PdCl₂ standard; Fit range $3 < k < 11.5$, $1 < R < 3$; no. of independent points = 11; (Pt sample) $S_0^2 = 0.91$ as deduced by Pt foil standard; Fit range $3.5 < k < 14$, $1 < R < 6$; no. of independent points = 32.

219 radial distribution function is indicative of metallic particles,
 220 and EXAFS data can be modeled by including the contribution
 221 from the nearest three Pt–Pt distances and a multiple
 222 scattering Pt–Pt path from the primary Pt coordination shell.
 223 The coordination number for the primary Pt coordination shell
 224 is smaller (8.4) than that expected for a bulk Pt structure (12),
 225 indicating the nanoparticulate nature of the Pt sample (Table
 226 1). In addition, by using an analogous EXAFS analysis, which
 227 was previously employed⁵⁰ for the calculation of particle sizes
 228 from CNs of the first shell of a face-centered cubic (fcc) system,
 229 we have estimated that our Pt NPs possess average diameters of
 230 1.4 nm. The EXAFS data of the reduced Pd sample is similar to
 231 the initial Pd precursor used for the preparation of the
 232 materials, with the largest contribution in the Fourier transform
 233 resulting from the primary Pd–Cl coordination shell. However,
 234 the EXAFS data also suggests the presence of Pd nanoparticles
 235 as indicated by a second feature in the imaginary part of the
 236 Fourier transform, which is consistent with a Pd–Pd scattering
 237 distance. The weak Pd–Pd contribution is evidence that only a
 238 small fraction of Pd sites are present as metallic species, with
 239 the majority of Pd sites consistent with the initial catalyst
 240 precursor. The radial distribution plot for the reduced Au
 241 sample is dominated by one component, which can be assigned
 242 to an Au–Cl scattering path. There is a good degree of
 243 correlation between the EXAFS data of the reduced Au sample
 244 and the KAuCl₄ precursor, indicating that the significant
 245 component in this reduced sample is the [AuCl₄][−] anion.
 246 Although there is no observable metallic contribution from the
 247 EXAFS data, some NP formation is clearly observed (see XPS
 248 and TEM data) and is present at least in a minor fraction. It is
 249 also noteworthy that the EXAFS data for the calcined material
 250 shows evidence of metallic Au (Figure S2.1); however, the
 251 similarity with the Au reference foil indicates mostly larger
 252 nanoparticles with more bulk properties.
 253 XAS data was also obtained for the calcined Pt and Pd
 254 materials (Figures S2.2, S2.3); however for the most part, due
 255 to XAS being a bulk analysis technique, the data for the Pt and
 256 Pd matched quite closely with the standards collected for the
 257 respective precursor chloride materials. This highlights the fact
 258 that only a small quantity of the chlorometallate anions have
 259 been extruded, in comparison with the reduced samples, to
 260 form nanoparticles. It is well-known that [AuCl₄][−] can be
 261 reduced thermally in the presence of any gas,⁵¹ which explains
 262 the presence of metallic species for the calcined Au material.
 263 However, the Pt and Pd materials require much more specific
 264 reducing conditions, as outlined in the Experimental Section,
 265 for the generation of nanoparticles.
 266 High-resolution XPS data were also acquired in order to
 267 further probe the nature of the metallic species, and to contrast

these findings with the XAS studies. As can be seen in the XPS 268
 spectra for the Au samples (Figure 3), a signal for Au(0) is 269

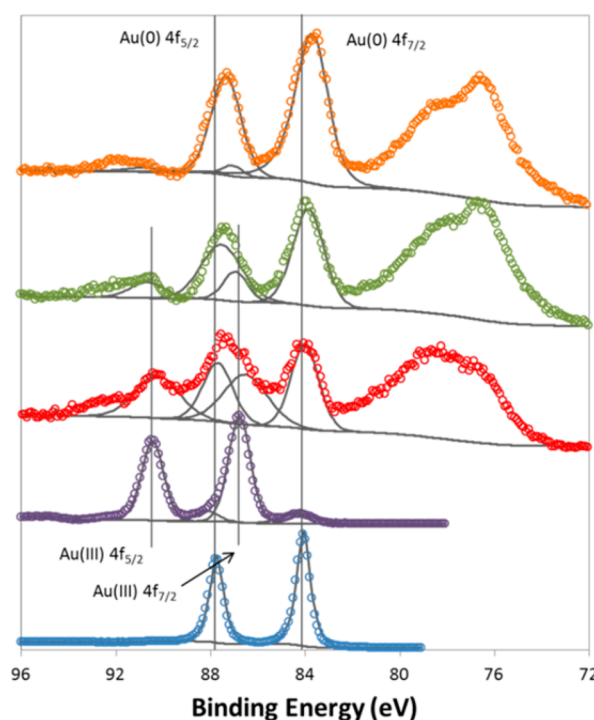


Figure 3. XPS spectra of metallic Au (blue circles) and KAuCl₄ (purple circles) standards, and as-synthesized (red circles), calcined (green circles) and reduced (orange circles) Au materials. (Black lines indicate background and component peaks.)

present not only in the reduced sample but also in the calcined 270
 and as-synthesized materials. It is highly likely that these are 271
 generated from small amounts of larger crystalline gold 272
 impurities in the synthesis procedure, before the actual 273
 formation of the crystalline framework. This is apparent from 274
 the observation that the Au(0) 4f_{7/2} signal has a binding energy 275
 that is typical of bulk gold at 84.1 eV. It was further noted in the 276
 calcined sample that the presence of the Au(0) signal increases 277
 relative to that of the Au(III) 4f_{7/2} signal at 86.8 eV, but a slight 278
 shift to lower binding energy for the Au(0) 4f_{7/2} to 83.9 eV was 279
 observed. Furthermore, for the reduced sample, almost 280
 complete conversion of Au(III) to Au(0) was observed, with 281
 a greater shift in the Au(0) 4f_{7/2} peak to a lower binding energy 282
 of 83.6 eV. This shift to a lower binding energy for the Au(0) 283
 peaks has been observed, as a notable characteristic, for the 284
 formation of nanoparticulate gold.^{52,53} Miller et al.⁵² attribute 285

286 this phenomenon to a change in the local electronic structure
287 close to the Fermi level of the small nanoparticles, in
288 comparison with bulk gold.

289 In stark contrast to XAS, XPS is a surface sensitive technique,
290 and thus, it is interesting to note the presence of metallic Au
291 NPs in the XPS, even though a larger proportion of the Au
292 present was shown to manifest as $[\text{AuCl}_4]^-$ from the EXAFS
293 measurements (Figure 2). Given that the sampling volume of
294 XPS analysis has a depth less than 10 nm and that the crystallite
295 sizes are approximately 20 μm ,⁷ these results indicate that our
296 materials are composed of isolated fractions of surface NPs and
297 hence represent distinct, discrete regions of Au species.

298 The large peak adjacent to the Au 4f peaks at lower binding
299 energy (76–78 eV) in the XPS spectra (Figure 3) is associated
300 with a Cu 3p signal originating from the framework. Although
301 this is clearly resolved from the Au peaks in Figure 3, there is
302 some overlap with the Pt 4f peaks, as can be seen in Figure 4.

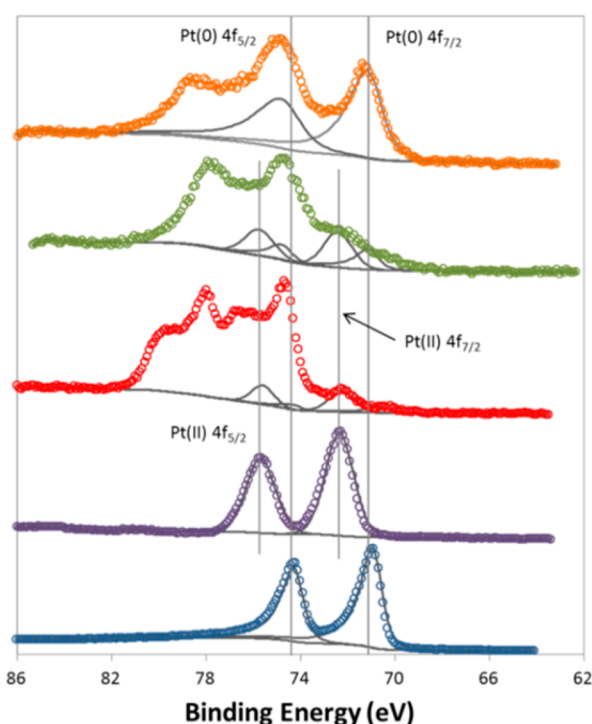


Figure 4. XPS spectra of metallic Pt standard (blue circles) and K_2PtCl_4 standard (purple circles), and as-synthesized (red circles), calcined (green circles), and reduced (orange circles) Pt materials. (Black lines indicate background and component peaks.)

303 For the sake of clarity, only peaks from the Pt have been
304 displayed in Figure 4 (see Figure S3.1 for an exemplar fitting
305 with Cu 3p assignments). From the Pt XPS data, we can
306 observe a similar trend to the Au materials; namely, calcination
307 of the as-synthesized Pt sample results in the generation of a
308 small quantities of Pt(0) that is apparent at 71.2 eV (compared
309 with Pt(II) at 72.4 eV). However, the most striking observation
310 was noted for the reduced sample (Figure 4), where the almost
311 complete reduction of the Pt(II) is apparent, with only peaks
312 associated with the metallic Pt(0) dominating the spectra.
313 These results, juxtaposed with observations from the EXAFS
314 data (Figure 2 and Table 1), further corroborate our findings
315 relating to the complete reduction of the $[\text{PtCl}_4]^{2-}$ species to
316 metallic NPs.

XPS data from the Pd 3d region of the spectra (Figure 5) 317
clearly show a transition from a mixture of Pd(IV) and Pd(II) 318

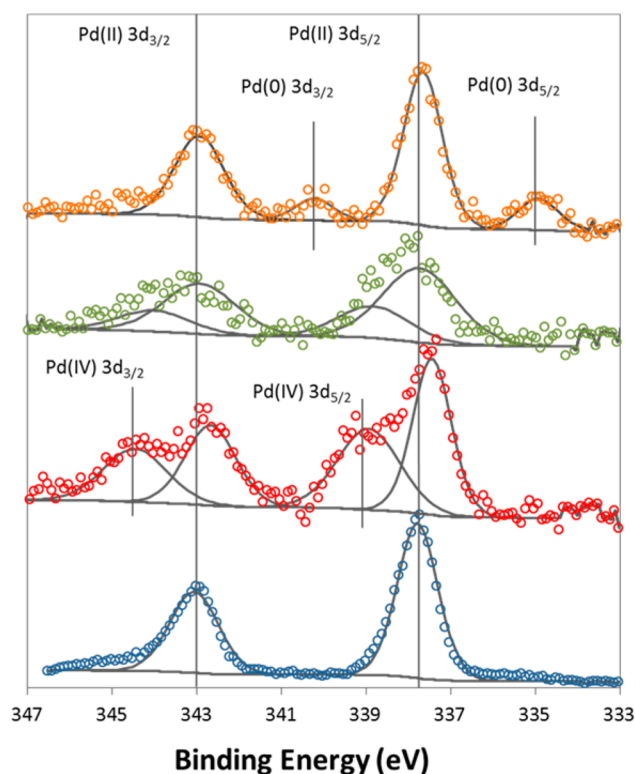


Figure 5. XPS spectra of K_2PdCl_4 standard (blue circles) and as-synthesized (red circles), calcined (green circles), and reduced (orange circles) Pd materials. (Black lines indicate background and component peaks.)

species in the as-synthesized material (binding energies of 338.9 319
and 337.6 eV respectively), to predominantly Pd(II) in the 320
calcined analogues, with some indications for the presence of 321
Pd(0) (335.0 eV), in the reduced samples. A clear contribution 322
of Pd(IV) was noted in some of our samples. A related study⁵⁴ 323
dealing with the location of supported Pt(II) species noted that, 324
in close proximity, a mixed valence Pt(II)–Pt(IV) bonded 325
dimer was formed, the presence of which was further 326
substantiated by DFT calculations. It is highly plausible that a 327
similar mechanism is operating in our systems, where mixed- 328
valence dimers are formed as precursors to cluster formation, 329
prior to nucleation and eventual nanoparticle growth. This, in 330
conjunction with the EXAFS data, clearly shows that, although 331
the reduction process seems to be much better for extruding 332
nanoparticles than calcination, the presence of metallic Pd(0) is 333
still minor, in comparison with Pd(II) species. We can also 334
conclude that the EXAFS data provide no evidence of any 335
significant PdO_x phase, with the major contribution in the 336
Fourier transform associated with the characteristic scattering 337
of Pd–Cl (Figure 2). EXAFS data was also acquired for a PdO 338
standard (Figure S2.4), which illustrates two distinct shells 339
(Pd–O and Pd–Pd scattering paths) in the Fourier transform, 340
that are not present in the data obtained for our Pd materials. 341
This supports our assertion that Pd oxide particles are not 342
produced during the synthesis procedure and that the Pd(II) 343
species are predominantly associated with the abundant 344
chlorometallate precursor anions, as in the as-synthesized 345
materials. 346

347 It is interesting to note that, although identical conditions
348 were used for thermally activating the analogous metalchloride
349 supported frameworks, the Pt material appears much more
350 readily amenable and susceptible to nanoparticle formation by
351 extrusion, than the Au or Pd. This could be attributed to the
352 differing strength of interactions between the discrete
353 chlorometallate anions within the framework channels and
354 the framework matrix. Further work is currently in progress to
355 study the calcination and reduction protocols in greater detail
356 using in situ X-ray absorption spectroscopy coupled with high-
357 resolution electron microscopy (using high-angle annular dark-
358 field imaging and tomography).

359 TEM analysis of the reduced catalysts are shown in Figure 6,
360 which reveal that the Au, Pt, and Pd catalyst frameworks are

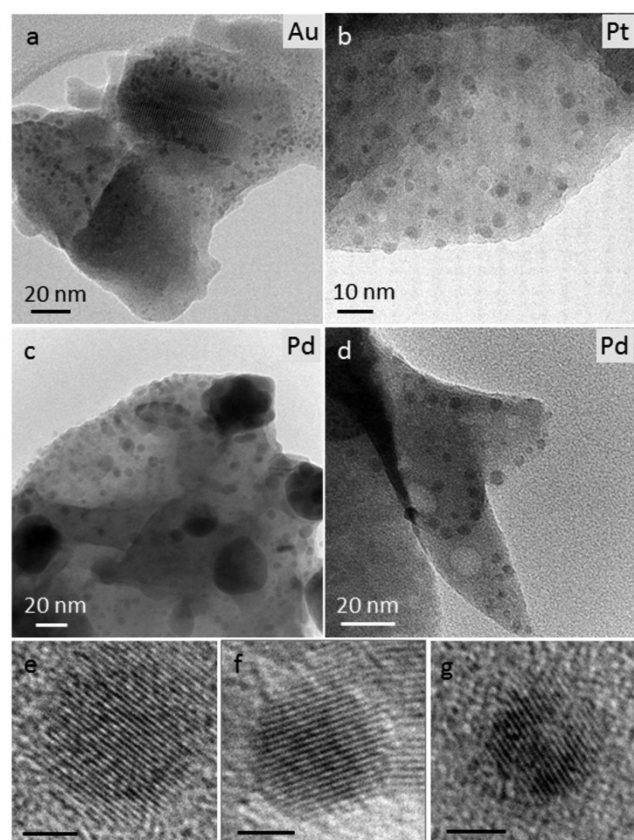


Figure 6. TEM images of reduced (a) Au, (b) Pt and (c)–(d) Pd catalysts, with magnified images of individual Au (e), Pt (f), and Pd (g) nanoparticles (scale bars in (e)–(g) are 2 nm).

361 composed of coexisting crystalline and amorphous phases. The
362 presence of crystalline embedded nanoparticles, with typical
363 diameters of 2–6 nm, can be seen in Figure 6b. High-resolution
364 TEM analysis, shown in Figure 6e,f, display particles with
365 measured fringe spacings of 0.2 and 0.23 nm, which can be
366 attributed to Au(200) and Pt(111), respectively.⁵⁵ The mean
367 diameter of the Pt NPs estimated from TEM is 2.6 nm (std dev
368 = 0.7) (Figure S4.1), which is slightly higher than that
369 estimated by analysis of the EXAFS data, but certainly in
370 agreement with overall particle sizes, which are less than 3 nm
371 across the bulk of the material. The sizes are smaller than that
372 previously reported for NPs extruded by calcination in air at
373 500 °C,⁷ with both the lower temperature and reducing
374 conditions favoring smaller NP formation. It should be noted,
375 however, that a thorough high-resolution TEM study was

hindered by the beam sensitivity of the catalysts. The
376 morphology of the reduced Pd catalysts shows some differences
377 compared to the Au and Pt catalysts, with the presence of larger
378 particles (20–50 nm) embedded in an amorphous matrix, as
379 shown in Figure 6c. Due to sensitivity (dynamic changes in
380 crystal orientation) of the sample under the electron beam,⁵⁶
381 the atomic resolution crystallinity of these particles could not
382 be probed in greater detail. However, there is evidence of some
383 Pd nanoparticle formation, as seen in Figure 6g, displaying
384 lattice fringes of 0.22 nm, characteristic of Pd(111).⁵⁵ The Pd
385 nanoparticles are innately located at the edges of the composite
386 material.

All three catalysts (calcined and reduced under identical
388 conditions, as outlined in the Experimental Section) were
389 probed for their catalytic potential, with a view to establishing
390 some initial trends that could be rationalized not only on the
391 basis of the shape and size of the nanoparticles but also, more
392 importantly, on their propensity to readily extrude from their
393 crystalline microporous framework. The aerobic oxidation of
394 vanillyl alcohol to vanillin, an intermediate step in the industrial
395 process to form vanillin from guaiacol (Schemes 2 and 3), was
396 used as a model probe reaction, given its importance from a
397 technological perspective. Interestingly, as reported in Figure
398 7a, all three reduced catalysts displayed high activities for this
399 7 aerobic oxidation, with the reduced Pt analogue affording close
400 to 100% conversion and selectivities for vanillin in excess of
401 80%, for this one-step process that we have devised (in contrast
402 with the multistep processes that are currently employed).
403 Given the challenging aspects of this aerobic oxidation,
404 turnover numbers (TONs) obtained with the Au and Pd
405 catalysts were modest. However, the performance of the
406 corresponding Pt analogue far exceeded that of its Au and Pd
407 counterparts, with the reduced Pt catalyst, to the best of our
408 knowledge, yielding unprecedented turnover values for this
409 aerobic oxidation at moderate reaction conditions (Figure 8).
410 8 This clearly highlights the superior role of the Pt NP catalyst, in
411 this series of materials, for aerobic oxidation reactions. From
412 the XPS and EXAFS data, the high activity of the Pt material
413 can be attributed to the complete extrusion of the [PtCl₄]²⁻
414 precursor, to yield stabilized discrete nanoparticles that are
415 amenable for catalysis, in stark contrast with the Au and Pd
416 materials (Figures 2 and 4).

The catalytic oxidation is composed of three main steps,
418 namely: (i) the adsorption of the alcohol on the surface with
419 the formation of a metal-alcoholate species; (ii) the β -hydride
420 elimination that results in the formation of the metal-hydride
421 intermediate and the carbonyl compound, which subsequently
422 desorbs; and (iii) the oxidation of the metal hydride
423 intermediate with concomitant formation of water and
424 subsequent regeneration of the metallic active site, which is
425 now available for further catalytic turnover.^{1,19,57} The resulting
426 product selectivity from the catalytic reaction is outlined in
427 Figure 7b, from where it is possible to distinguish different
428 trends, in relation to the specific examined catalyst. The
429 reduced Pt catalyst affords the highest vanillin selectivity
430 (>80%), which is relatively consistent, except for the formation
431 of a small quantities of vanillic acid after prolonged contact
432 times. The vanillin selectivity for the reduced Pd material
433 increases steadily over time, but the corresponding reduced Au
434 catalyst displays a distinctly different behavior compared to the
435 others, with the selectivity toward vanillin decreasing
436 monotonically with reaction time. The formation of the
437 byproduct 4-hydroxy-3-methoxybenzyl *tert*-butyl ether was
438

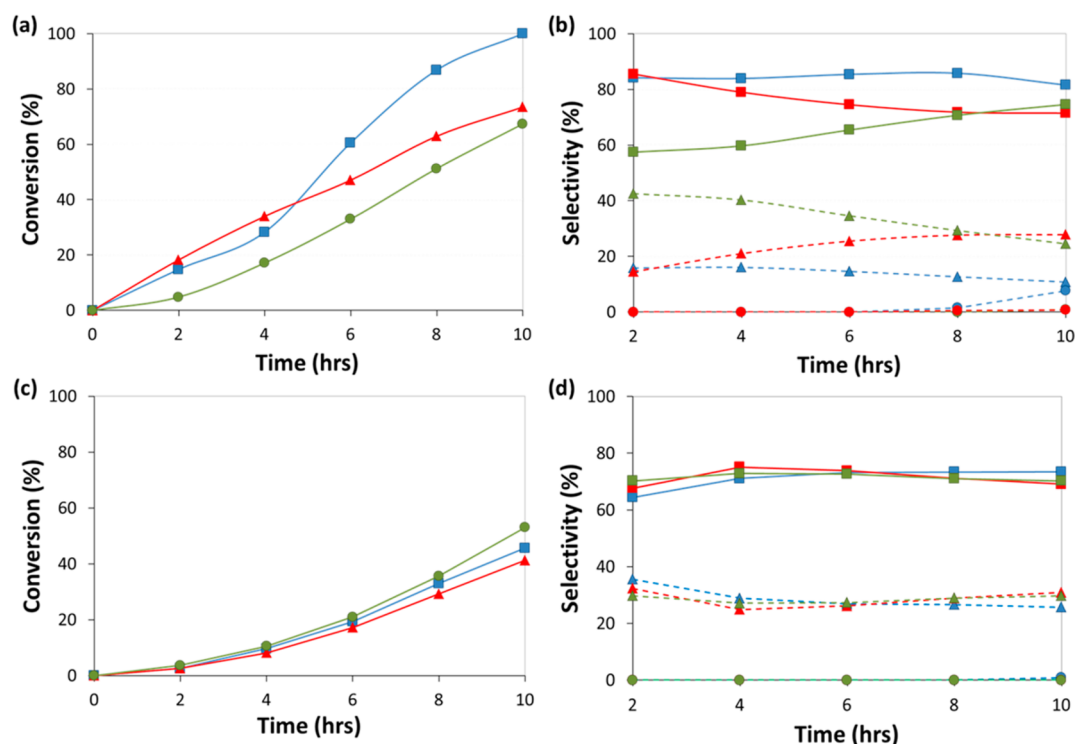


Figure 7. Kinetic plots outlining the catalytic activity for the Au (red triangles), Pt (blue squares), and Pd (green circles) reduced (a) and calcined catalysts (c). Corresponding selectivity profiles of Au (red), Pt (blue), and Pd (green) reduced (b) and calcined catalysts (d) toward vanillin (squares), 4-hydroxy-3-methoxybenzyl *tert*-butyl ether (triangles), and vanillic acid (circles). Reaction conditions: vanillyl alcohol (1 g), *tert*-butanol (30 mL), diglyme (0.85 g), catalyst (50 mg), $T = 170\text{ }^{\circ}\text{C}$, $P_{\text{air}} (20\text{ }^{\circ}\text{C}) = 20\text{ bar}$.

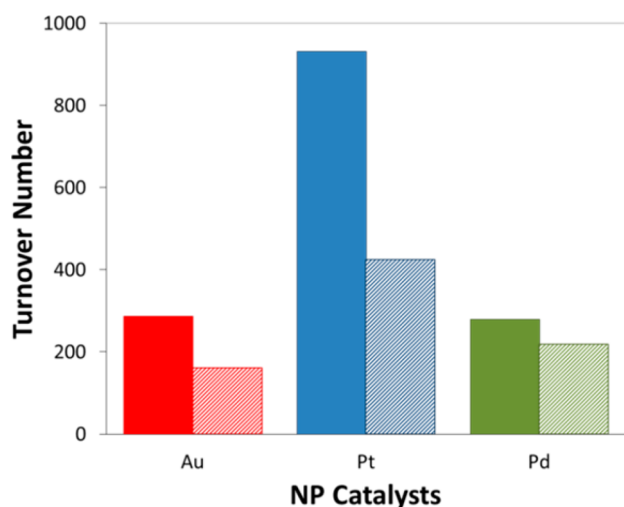
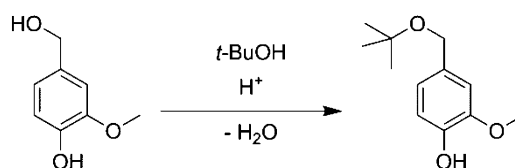


Figure 8. Comparison of catalytic turnover for Au (red), Pt (blue), and Pd (green) reduced (solid) and calcined (patterned) catalysts. See Figure 7 for reaction conditions.

Scheme 4. Etherification of Vanillin with *t*-Butanol To Form Byproduct



this is known for Au systems,^{57,58} it is highly likely that similar mechanisms are also facilitating the formation of this product (4-hydroxy-3-methoxybenzyl *tert*-butyl ether) for the Pt and Pd catalysts, though with varying kinetics of hydride formation, which accounts for the different selectivities observed with these catalysts, when compared to the Au analogue. Detailed kinetic analyses are currently ongoing, and these will be published separately.

In order to investigate the effect of temperature on the catalytic activity of the materials, analogous reactions were performed at $150\text{ }^{\circ}\text{C}$. In line with our expectations, the lower temperatures afforded reduced activity but more importantly resulted in a comparatively higher selectivity toward the ether product (Table 2). It was indeed revealing that lower reaction temperatures facilitated the stabilization of the metal–alcoholate complex, thereby inducing a higher propensity for etherification. In addition to this, the adsorption stability of the formed aldehyde was higher at lower reaction temperatures, leading to longer induction periods in the catalysis. However, the reduced Pt catalyst again affords the highest selectivity toward the target product (vanillin), when compared to the Au and Pd analogues, despite its activity being drastically inferior when compared to the catalytic tests at $170\text{ }^{\circ}\text{C}$ (Figure 7a).

confirmed using gas chromatography-mass spectrometry (GC-MS) analysis, and it was noted that the selectivity for this particular product increases over time for the Au catalyst. The origin of the 4-hydroxy-3-methoxybenzyl *tert*-butyl ether can be readily rationalized on the basis of the generation of a hydride species,^{57,58} that induces local acidity in the nanoparticle, thus facilitating the etherification between the stabilized vanillyl alcoholate and the adsorbed *tert*-butanol solvent molecules (Scheme 4). It is well-known that *p*-hydroxybenzylic alcohols can undergo an etherification reaction in presence of another alcohol under acidic or harsh oxidative conditions.⁵⁹ Although

Table 2. Kinetic Data for the Aerobic Oxidation of Vanillyl Alcohol at 150 °C^a

metal	time (h)	conv. (%)	selectivity (%)			TON ^d
			vanillin	ether ^b	acid ^c	
Pt	8	14.35	74.15	25.85	0	133
	10	32.25	76.00	24.00	0	298
Au	8	35.79	54.06	45.94	0	140
	10	42.03	55.61	44.39	0	164
Pd	8	24.11	51.41	48.59	0	99
	10	32.38	52.83	47.17	0	133

^aFor reaction conditions (excluding temperature), see Figure 7. ^b4-hydroxy-3-methoxybenzyl *tert*-butyl ether. ^cVanillic acid. ^dTON based on conversion of vanillyl alcohol.

473 Thus, in order to maximize both conversions and selectivities to
474 the desirable vanillin, higher reaction temperatures must be
475 employed in this particular system.

476 Analogous reactions were also carried out with the calcined
477 catalysts, in order to make reactivity/selectivity comparisons
478 with those of the reduced counterparts described in Figure 7a,b.
479 As can be seen from Figure 7c,d, there is very little difference in
480 the reactivity and selectivity profiles for all three catalysts. It is
481 however significant that the latter (calcined catalysts) are
482 markedly inferior in catalytic performance when compared with
483 their reduced analogues, which further indicates the superior
484 performance of the reduced materials, and in particular the Pt
485 catalyst. The catalytic performance of these materials can
486 indeed be rationalized from the XPS data (Figure 4), which
487 reveals an enhancement in the *metallic* character of the reduced
488 Pt catalyst, which are clearly the desired active sites for this
489 aerobic oxidation reaction. Consistent with the above, the
490 pronounced increase in activity for the reduced Au catalyst,
491 when compared with its calcined analogue, can also be
492 corroborated from the detection of higher quantities of
493 nanoparticulate gold, as confirmed from the shift in the binding
494 energies in the XPS spectra (Figure 3). It was therefore
495 unsurprising to note that only a marginal difference was
496 observed in the catalytic activity of the reduced Pd catalyst,
497 when compared with its calcined counterpart, as only a very
498 small proportion of metallic Pd was detected by XPS (and
499 TEM), with the EXAFS analysis predominantly revealing the
500 presence of the precursor ($[\text{PdCl}_4]^{2-}$) species, postreduction.

501 There are very few reports on the use of NP catalysts for the
502 aerobic oxidation of vanillyl alcohol to vanillin. However, the
503 use of Pt/MOF-5⁶⁰ and Pt/C⁶¹ were recently shown to have
504 some activity, but with low TOFs of 4.9 h⁻¹ and 19 h⁻¹
505 respectively, in comparison with 93 h⁻¹ achieved with our
506 reduced Pt/CuClP material. Other recent studies have explored
507 the use of Co catalysts to catalyze the aerobic oxidation of
508 vanillyl alcohol,^{62,63} although the use of a base was mandatory
509 in these systems. In these studies,^{62,63} conversion and selectivity
510 toward vanillin appear promising; however, the low substrate to
511 catalyst ratios employed result in inferior TONs at complete
512 conversion. The superior TONs displayed by these extruded
513 catalysts and, in particular, the reduced Pt nanoparticles (Figure
514 8), which afford TON/TOFs that are at least 4 times higher
515 than existing Pt NP catalysts and almost two-orders of
516 magnitude greater than other transition metal systems (to the
517 best of our knowledge), offers adequate scope for the industrial
518 implementation of these catalysts for the production of vanillin
519 through benign, aerobic oxidation routes.

SUMMARY AND FUTURE PROSPECTS

520

521 It has been shown that the $[\text{PtCl}_4]^{2-}$ supported porous copper
522 chlorophosphate framework is highly susceptible to complete
523 extrusion by reduction, forming isolated, discrete nanoparticles,
524 which are the loci for aerobic oxidation reactions. The
525 propensity of the Pt NPs to readily extrude from within the
526 porous architecture offers a unique strategy for the design of
527 single-site heterogeneous catalysts, where the nature of the
528 active site can be dexterously manipulated and controlled
529 through judicious activation procedures. The design approach
530 has also facilitated the structural (XRD, EXAFS, TEM) and
531 spectroscopic (XPS, XAS) characterization of the active sites at
532 a molecular level, which have proved invaluable in facilitating
533 structure–property correlations for understanding the implica-
534 tions of the superior activity afforded by reduced Pt particles for
535 the aerobic oxidation of vanillyl alcohol to vanillin.

536 The study has further established that analogous precursors
537 for generating Au and Pd nanoparticles are sensitive to the
538 thermal activation procedures that are employed, which in turn
539 has a critical influence on the ensuing catalysis. It has been
540 found that reduction procedures under H₂ are more effective
541 than calcinations for extruding the chlorometallate precursors
542 in all three catalysts, but with distinct and varying influences
543 that directly affect the catalytic turnover. While we have
544 identified an efficient route for generating Pt NPs by this route,
545 further studies (currently in progress) will pinpoint activation
546 methodologies that favor complete extrusion of the analogous
547 Au and Pd catalysts.

548 It is envisaged that this initial investigation will pave the way
549 for further exploring and exploiting the potential of this novel
550 extrusion strategy for generating new nanoparticle catalysts. By
551 using a combination of in situ and operando tools for directly
552 probing the nature of the active site during the activation
553 procedure will afford a greater understanding of how each metal
554 within the framework responds to thermal treatments. This
555 would help establish a detailed understanding of size/shape
556 distributions, compositional integrity, and, more importantly,
557 precise location of the extruded nanoparticles, which could, in
558 turn, facilitate a design-application approach for the controlled
559 engineering of superior catalysts for a wider-range of
560 industrially significant catalytic transformations.

ASSOCIATED CONTENT

561

Supporting Information

562

563 The Supporting Information is available free of charge on the
564 ACS Publications website at DOI: 10.1021/acscatal.5b00481.

565 Industrial process schemes, EXAFS spectra, XPS data,
566 TEM particle size distribution (PDF)

AUTHOR INFORMATION

567

Corresponding Author

568

*E-mail: R.Raja@soton.ac.uk. Tel: (+44)23 8059 2144.

569

Notes

570

571 The authors declare no competing financial interest.

ACKNOWLEDGMENTS

572

573 X-ray photoelectron spectra were obtained at the National
574 EPSRC XPS User's Service (NEXUS) at Newcastle University,
575 an EPSRC Mid-Range Facility. We would like to especially
576 thank Dr. Naoko Sano at the NEXUS XPS facility for his help
577 in collecting XPS data and his invaluable advice for data

578 analysis. We thank Diamond Light Source for access to
579 beamline B18 (SP8071-6) that contributed to the results
580 presented here. U.K. Catalysis Hub is kindly thanked for
581 resources and support provided via our membership of the U.K.
582 Catalysis Hub Consortium and funded by EPSRC (portfolio
583 grants EP/K014706/1, EP/K014668/1, EP/K014854/1 and
584 EP/K014714/1). C.S.H. thanks the University of Southampton
585 for a VC scholarship and A*STAR, Singapore for funding
586 under the ARAP award scheme. J.D.H./G.C. acknowledge
587 financial support from Science Foundation Ireland (Grant: 08/
588 CE/I1432) and instrument support from the Electron
589 Microscopy and Analysis Facility (EMAF) at Tyndall.

590 ■ REFERENCES

- 591 (1) Davis, S. E.; Ide, M. S.; Davis, R. J. *Green Chem.* **2013**, *15*, 17–45.
592 (2) Dimitratos, N.; Lopez-Sanchez, J. A.; Anthonykuty, J. M.; Brett,
593 G.; Carley, A. F.; Tiruvalam, R. C.; Herzing, A. A.; Kiely, C. J.; Knight,
594 D. W.; Hutchings, G. J. *Phys. Chem. Chem. Phys.* **2009**, *11*, 4952–4961.
595 (3) Enache, D. I.; Edwards, J. K.; Landon, P.; Solsona-Espriu, B.;
596 Carley, A. F.; Herzing, A. A.; Watanabe, M.; Kiely, C. J.; Knight, D. W.;
597 Hutchings, G. J. *Science* **2006**, *311*, 362–365.
598 (4) Balcha, T.; Strobl, J. R.; Fowler, C.; Dash, P.; Scott, R. W. J. *ACS*
599 *Catal.* **2011**, *1*, 425–436.
600 (5) MacLennan, A.; Banerjee, A.; Hu, Y.; Miller, J. T.; Scott, R. W. J.
601 *ACS Catal.* **2013**, *3*, 1411–1419.
602 (6) Chen, H. W.; Murugadoss, A.; Hor, T. S. A.; Sakurai, H. *Molecules*
603 **2010**, *16*, 149–161.
604 (7) Hinde, C. S.; Van Aswegen, S.; Collins, G.; Holmes, J. D.; Hor, T.
605 S. A.; Raja, R. *Dalton Trans.* **2013**, *42*, 12600–12605.
606 (8) Kesavan, L.; Tiruvalam, R.; Rahim, M. H. A.; bin Saiman, M. I.;
607 Enache, D. I.; Jenkins, R. L.; Dimitratos, N.; Lopez-Sanchez, J. A.;
608 Taylor, S. H.; Knight, D. W.; Kiely, C. J.; Hutchings, G. J. *Science* **2011**,
609 *331*, 195–199.
610 (9) bin Saiman, M. I.; Brett, G. L.; Tiruvalam, R.; Forde, M. M.;
611 Sharples, K.; Thetford, A.; Jenkins, R. L.; Dimitratos, N.; Lopez-
612 Sanchez, J. A.; Murphy, D. M.; Bethell, D.; Willock, D. J.; Taylor, S.
613 H.; Knight, D. W.; Kiely, C. J.; Hutchings, G. J. *Angew. Chem., Int. Ed.*
614 **2012**, *51*, 5981–5985.
615 (10) Collins, G.; Blömker, M.; Osiak, M.; Holmes, J. D.; Bredol, M.;
616 O'Dwyer, C. *Chem. Mater.* **2013**, *25*, 4312–4320.
617 (11) Chen, Y.-X.; Lavacchi, A.; Chen, S.-P.; di Benedetto, F.;
618 Bevilacqua, M.; Bianchini, C.; Fornasiero, P.; Innocenti, M.; Marelli,
619 M.; Oberhauser, W.; Sun, S.-G.; Vizza, F. *Angew. Chem., Int. Ed.* **2012**,
620 *51*, 8500–8504.
621 (12) Cheong, S.; Watt, J. D.; Tilley, R. D. *Nanoscale* **2010**, *2*, 2045–
622 2053.
623 (13) Henning, A. M.; Watt, J.; Miedziak, P. J.; Cheong, S.;
624 Santonastaso, M.; Song, M.; Takeda, Y.; Kirkland, A. I.; Taylor, S.
625 H.; Tilley, R. D. *Angew. Chem., Int. Ed.* **2013**, *52*, 1477–1480.
626 (14) Strizhak, P. E. *Theor. Exp. Chem.* **2013**, *49*, 2–21.
627 (15) Barau, A.; Budarin, V.; Caragheorghopol, A.; Luque, R.;
628 Macquarrie, D.; Prella, A.; Teodorescu, V.; Zaharescu, M. *Catal. Lett.*
629 **2008**, *124*, 204–214.
630 (16) Haruta, M.; Tsubota, S.; Kobayashi, T.; Kageyama, H.; Genet,
631 M. J.; Delmon, B. J. *Catal.* **1993**, *144*, 175–192.
632 (17) Dimitratos, N.; Villa, A.; Wang, D.; Porta, F.; Su, D.; Prati, L. J.
633 *Catal.* **2006**, *244*, 113–121.
634 (18) Porta, F.; Prati, L.; Rossi, M.; Scari, G. J. *Catal.* **2002**, *211*, 464–
635 469.
636 (19) Abad, A.; Corma, A.; Garcia, H. *Chem. - Eur. J.* **2008**, *14*, 212–
637 222.
638 (20) Raja, R.; Hermans, S.; Shephard, D. S.; Johnson, B. F. G.; Raja,
639 R.; Sankar, G.; Bromley, S.; Thomas, J. M. *Chem. Commun.* **1999**,
640 1571–1572.
641 (21) Adams, R. D.; Boswell, E. M.; Captain, B.; Hungria, A. B.;
642 Midgley, P. A.; Raja, R.; Thomas, J. M. *Angew. Chem., Int. Ed.* **2007**, *46*,
643 8182–8185.
(22) Gianotti, E.; Shetti, V. N.; Manzoli, M.; Blaine, J. A. L.; Pearl, W. 644
C.; Adams, R. D.; Coluccia, S.; Raja, R. *Chem. - Eur. J.* **2010**, *16*, 8202– 645
8209. 646
(23) Raja, R.; Khimiyak, T.; Thomas, J. M.; Hermans, S.; Johnson, B. 647
F. G. *Angew. Chem., Int. Ed.* **2001**, *40*, 4638–4642. 648
(24) Hungria, A. B.; Raja, R.; Adams, R. D.; Captain, B.; Thomas, J. 649
M.; Midgley, P. A.; Golovko, V.; Johnson, B. F. G. *Angew. Chem., Int.* 650
Ed. **2006**, *45*, 4782–4785. 651
(25) Raja, R.; Adams, R. D.; Blom, D. A.; Pearl, W. C.; Gianotti, E.; 652
Thomas, J. M. *Langmuir* **2009**, *25*, 7200–7204. 653
(26) Zheng, N.; Stucky, G. D. *J. Am. Chem. Soc.* **2006**, *128*, 14278– 654
14280. 655
(27) Tasis, D.; Tagmatarchis, N.; Bianco, A.; Prato, M. *Chem. Rev.* 656
2006, *106*, 1105–1136. 657
(28) Laursen, A. B.; Højholt, K. T.; Lundegaard, L. F.; Simonsen, S. 658
B.; Helveg, S.; Schüth, F.; Paul, M.; Grunwaldt, J.-D.; Kegnaes, S.; 659
Christensen, C. H.; Egeblad, K. *Angew. Chem., Int. Ed.* **2010**, *49*, 3504– 660
3507. 661
(29) Zhang, X.; Ke, X.; Zhu, H. *Chem. - Eur. J.* **2012**, *18*, 8048–8056. 662
(30) Lu, G.; Li, S.; Guo, Z.; Farha, O. K.; Hauser, B. G.; Qi, X.; 663
Wang, Y.; Wang, X.; Han, S.; Liu, X.; DuChene, J. S.; Zhang, H.; 664
Zhang, Q.; Chen, X.; Ma, J.; Loo, S. C. J.; Wei, W. D.; Yang, Y.; Hupp, 665
J. T.; Huo, F. *Nat. Chem.* **2012**, *4*, 310–316. 666
(31) Esken, D.; Turner, S.; Lebedev, O. I.; Van Tendeloo, G.; 667
Fischer, R. A. *Chem. Mater.* **2010**, *22*, 6393–6401. 668
(32) White, R. J.; Luque, R.; Budarin, V. L.; Clark, J. H.; Macquarrie, 669
D. J. *Chem. Soc. Rev.* **2009**, *38*, 481–494. 670
(33) Cheetham, A. K.; Férey, G.; Loiseau, T. *Angew. Chem., Int. Ed.* 671
1999, *38*, 3268–3292. 672
(34) Leithall, R. M.; Shetti, V. N.; Maurelli, S.; Chiesa, M.; Gianotti, 673
E.; Raja, R. *J. Am. Chem. Soc.* **2013**, *135*, 2915–2918. 674
(35) Thomas, J. M.; Raja, R. *Chem. Commun.* **2001**, 675–687. 675
(36) Thomas, J. M. *Proc. R. Soc. London, Ser. A* **2012**, *468*, 1884– 676
1903. 677
(37) Huang, Q.; Ulutagay, M.; Michener, P. A.; Hwu, S.-J. *J. Am.* 678
Chem. Soc. **1999**, *121*, 10323–10326. 679
(38) Williams, E. R.; Leithall, R. M.; Raja, R.; Weller, M. T. *Chem.* 680
Commun. **2013**, *49*, 249–251. 681
(39) Fahlbusch, K.-G.; Hammerschmidt, F.-J.; Panten, J.; 682
Pickenhagen, W.; Schatkowski, D.; Bauer, K.; Garbe, D.; Surburg, H. 683
Flavors and Fragrances. *Ullmann's Encyclopedia of Industrial Chemistry*, 684
7th ed.; Wiley-VCH Verlag GmbH & Co. KGaA: Weinheim, 2003; 685
Vol. 15, pp 73–198. 686
(40) Vidal, J.-P. Vanillin. *Kirk-Othmer Encyclopedia of Chemical* 687
Technology; John Wiley & Sons, Inc.: New York, 2006; pp 1–14. 688
(41) Metivier, P. Method for preparing a 4-hydroxybenzaldehyde and 689
derivatives. U.S. Patent No. 6,184,421 B1, February 6, 2001. 690
(42) Hansen, J.; Hansen, E. H.; Sompalli, H. P.; Sheridan, J. M.; Heal, 691
J. R.; Hamilton, W. D. O. Compositions and methods for the 692
biosynthesis of vanillin or vanillin beta-d-glucoside. Patent No. WO 693
2013022881 A1, April 3, 2013. 694
(43) Frost, J. W. Synthesis of vanillin from a carbon source. U.S. 695
Patent No. US 6372461 B1, 2002. 696
(44) Zope, B. N.; Hibbitts, D. D.; Neurock, M.; Davis, R. J. *Science* 697
2010, *330*, 74–78. 698
(45) Sheldon, R. A. *Chem. Soc. Rev.* **2012**, *41*, 1437–1451. 699
(46) Arends, I. W. C. E.; Sheldon, R. A.; Backvall, J.-E. Modern 700
Oxidation of Alcohols Using Environmentally Benign Oxidants. In 701
Modern Oxidation Methods; Backvall, J.-E., Ed.; Wiley-VCH: 702
Weinheim, 2005; pp 83–118. 703
(47) Fairley, N.; Carrick, A. *The Casa Cookbook*; Acolyte science: 704
Cheshire, U.K., 2005; pp 1–368. 705
(48) Newville, M. J. *Synchrotron Radiat.* **2001**, *8*, 322–324. 706
(49) Ravel, B.; Newville, M. J. *Synchrotron Radiat.* **2005**, *12*, 537– 707
541. 708
(50) Beale, A. M.; Weckhuysen, B. M. *Phys. Chem. Chem. Phys.* **2010**, 709
12, 5562–5574. 710

- 711 (51) *Catalysis by Gold*; Bond, G. C.; Louis, C.; Thompson, D. T.,
712 Eds.; Catalytic Science Series; Hutchings, G. J., Series Ed; Imperial
713 College Press: London, UK, 2006; Vol. 6, pp 1–383.
- 714 (52) Miller, J. T.; Kropf, A. J.; Zha, Y.; Regalbuto, J. R.; Delannoy, L.;
715 Louis, C.; Bus, E.; van Bokhoven, J. A. *J. Catal.* **2006**, *240*, 222–234.
- 716 (53) Turner, M.; Golovko, V. B.; Vaughan, O. P. H.; Abdulkin, P.;
717 Berenguer-Murcia, A.; Tikhov, M. S.; Johnson, B. F. G.; Lambert, R.
718 M. *Nature* **2008**, *454*, 981–983.
- 719 (54) Li, C.; Wang, Y.; Guo, X.; Jiang, Z.; Jiang, F.; Zhang, W.; Zhang,
720 W.; Fu, H.; Xu, H.; Wu, G. *J. Phys. Chem. C* **2014**, *118*, 3140–3144.
- 721 (55) Tan, Y. W.; Dai, X. H.; Li, Y. F.; Zhu, D. B. *J. Mater. Chem.*
722 **2003**, *13*, 1069–1075.
- 723 (56) Diaz, C.; Valenzuela, M. L.; Bravo, D.; Dickinson, C.; O'Dwyer,
724 C. *J. Colloid Interface Sci.* **2011**, *362*, 21–32.
- 725 (57) Ng, Y. H.; Ikeda, S.; Morita, Y.; Harada, T.; Ikeue, K.;
726 Matsumura, M. *J. Phys. Chem. C* **2009**, *113*, 12799–12805.
- 727 (58) Wang, X.; Andrews, L. *Angew. Chem., Int. Ed.* **2003**, *42*, 5201–
728 5206.
- 729 (59) Ramu, R.; Ravindra Nath, N.; Reddy, M. R.; Das, B. *Synth.*
730 *Commun.* **2004**, *34*, 3135–3145.
- 731 (60) Tarasov, A. L.; Kustov, L. M.; Isaeva, V. I.; Kalenchuk, A. N.;
732 Mishin, I. V.; Kapustin, G. I.; Bogdan, V. I. *Kinet. Catal.* **2011**, *52*,
733 273–276.
- 734 (61) Tarasov, A. L.; Kustov, L. M.; Bogolyubov, A. A.; Kiselyov, A. S.;
735 Semenov, V. V. *Appl. Catal., A* **2009**, *366*, 227–231.
- 736 (62) Zakzeski, J.; Dębczak, A.; Bruijninx, P. C. A.; Weckhuysen, B.
737 M. *Appl. Catal., A* **2011**, *394*, 79–85.
- 738 (63) Garade, A. C.; Biradar, N. S.; Joshi, S. M.; Kshirsagar, V. S.; Jha,
739 R. K.; Rode, C. V. *Appl. Clay Sci.* **2011**, *53*, 157–163.